PET image reconstruction: A stopping rule for the MLEM algorithm based on properties of the updating coefficients

Anastasios Gaitanis [f,b,1], George Kontaxakis [d,e,2], George Spyrou [b,3], George Panayiotakis [f,4], George Tzanakos [a,c,*]

[a] University of Athens, Department of Physics, Division of Nuclear & Particle Physics, Panepistimioupoli, Zografou, Athens 15771, Greece
[b] Biomedical Research Foundation of the Academy of Athens (BRFAA), Soranou Efessiou 4, Athens 11527, Greece
[c] University of Cyprus, Department of Physics, Faculty of Pure and Applied Sciences, Nicosia 1678, P.O. Box 20537, Cyprus
[d] Universidad Politécnica de Madrid, E.T.S.I. Telecomunicación, Dpto. Ingeniería Electrónica, 28040 Madrid, Spain
[e] Networking Research Center on Bioengineering, Biomaterials and Nanomedicine (CIBER-BBN), Madrid, Spain
[f] Department of Medical Physics, Medical School, University of Patras, 265 00 Patras, Greece

ARTICLE INFO

ABSTRACT

An empirical stopping criterion for the 2D-maximum-likelihood expectation–maximization (MLEM) iterative image reconstruction algorithm in positron emission tomography (PET) has been proposed. We have applied the MLEM algorithm on Monte Carlo generated noise-free projection data and studied the properties of the pixel updating coefficients (PUC) in the reconstructed images. Appropriate fitting lead to an analytical expression for the parameterization of the minimum value in the PUC vector for all non-zero pixels for a given number of detected counts, which can be employed as basis for the stopping criterion proposed. These results have been validated with simulated data from real PET images.

© 2009 Elsevier Ltd. All rights reserved.

1. Introduction

Positron emission tomography (PET) imaging is currently used in a wide area of medical disciplines, such as oncology, neurology, cardiology, as well as in pre-clinical research and drug development [1–4]. Image reconstruction plays an important role on the quality of the images produced by a PET camera [5]. Modern PET scanners employ iterative image reconstruction algorithms such as the maximum-likelihood expectation–maximization (MLEM) [6] and ordered subsets expectation–maximization (OSEM) [7] algorithms as well as several of their variants [8]. The MLEM algorithm has attracted considerable interest in the area of emission tomography, as it produces images with better quality than other techniques. However in practice, these iterative methods are computationally intensive and lack robust stopping criteria. A stopping criterion is essential because images produced in PET with MLEM algorithm have been observed to become noisier as iterations proceed. The modern PET image reconstruction methods either apply a regularization approach in order to maintain the level of noise in the images at a constrained level and repeat the process for an arbitrary number of iterations, or stop the iteration algorithm (MLEM or OSEM) after several iterations and then apply a filtering method in the reconstructed image [9]. From the literature however the existence and use of a robust stopping criterion for this iterative method is absent.

The issue of image reconstruction in emission tomography can be regarded as a statistical estimation problem. The MLEM

* Corresponding author. Tel.: +30 210 7276938; fax: +30 210 7276987.
  E-mail addresses: agaitanis@bioacademy.gr (A. Gaitanis), gkont@die.upm.es (G. Kontaxakis), gspyrou@bioacademy.gr (G. Spyrou), panayiot@upatras.gr (G. Panayiotakis), tzanakos@phys.uoa.gr (G. Tzanakos).
  [1] Tel: +30 210 6597318; fax: +30 210 6597629.
  [2] Tel.: +34 91 3367366; fax: +34 91 3367323.
  [3] Tel: +30 210 6597151; fax: +30 210 6597545.
  [4] Tel: +30 2610 996113; fax: +30 2610 996113.

algorithm provides an iterative formula to solve the problem of image reconstruction in PET using maximum-likelihood estimation (MLE) techniques by maximizing the probability to observe the given counts represented by the vector ȳ corresponding to the true activity distribution x̄ in the source, under a Poisson probability model for the positron emission proposed by Shepp and Vardi [6]. The MLEM algorithm produces images with fewer artefacts than other analytical methods, such as filtered back-projection (FBP), it can use an incomplete data set and does not require equally spaced projection data [10].

Many researchers have developed and proposed various stopping rules for the MLEM algorithm. Veklerov and Llacer [11] proposed a quantitative criterion with a simple probabilistic interpretation that allows the user to stop the algorithm just before the effect of deterioration begins. The 2D image is reconstructed using the MLEM algorithm and a parameter H is calculated at each iteration. This parameter is a part of the Pearson's χ^2 test. When the parameter H reaches its minimum value, the image quality is supposed to be optimal. The same authors in another paper [12] studied a stopping criterion based on a figure of merit (FOM) similar to the root mean squared (RMS) error and the reconstruction algorithm was stopped when this FOM reached its minimum value. This stopping criterion was tested using real data produced by a brain PET scanner. Furthermore, Holte et al. [13] studied a stopping rule based on the calculation of a parameter that takes into account the pixel values of the initial and reconstructed image. This parameter is taking into consideration the properties of the reconstructed image and its minimum value defines the optimum image quality. Recently, Bissantz et al. [14] proposed a method to calculate a stopping rule for MLEM algorithm based on an analysis that takes into consideration the residuals between the forward projected image and the measured counts for each row of the sinograms. Up to now, however, none of these proposed approaches have been proven of practical value for application in the clinical routine for PET studies.

The present paper deals with the problem of defining a stopping rule for the MLEM algorithm that is independent on the characteristics of the reconstructed image. For this purpose, we take into consideration the statistical behavior of the MLEM algorithm and focus on the study of its pixel updating coefficients (PUC). Studies of the behavior of these coefficients are absent from the literature except for some initial work published by our group [15–17]. In contrast to previously proposed methods, this approach focuses on the behavior of the pixel updating coefficients of the MLEM algorithm, which is shown here to be independent on the reconstructed images and their characteristics.

In the next sections, the basic methodology employed for this work is presented, with emphasis to the figures of merit employed here for the image quality estimation. Section 3 presents the main results of the study on the pixel updating coefficients vector, focusing on the properties of its minimum value for the non-zero pixels in the reconstructed image. A correlation study for this value with the image topology and activity distribution levels in the source is performed, leading to a quantitative expression that can be used to formulate an empirical stopping criterion for the iterative image reconstruction algorithm employed. Finally, a validation step of the proposed stopping rule is performed using simulated data from real scanned PET images from a mouse phantom.

2. Materials and methods

2.1. The PET scanner model

A single-ring PET camera has been modeled with 128 scintillation crystals on the ring, a detector width of 7.36 mm and a field of view (FOV) of 200 mm × 200 mm. The detector ring radius is 150 mm. The total number of detector pairs in coincidence is 8128. Several image sizes have been studied:

(a) 64 × 64 (pixel size = 3.12 mm),
(b) 128 × 128 (pixel size = 1.56 mm),
(c) 256 × 256 (pixel size = 0.78 mm) and
(d) 512 × 512 (pixel size = 0.39 mm).

For the simulation of the operation of the scanner, Monte Carlo methods were used; Firstly, the distribution of annihilation events into a pixel and secondly, the production of gamma rays and their detection by the detectors were simulated. The detector efficiency was assumed to be 100%. Compton scattering or photoelectric effects were not taken into consideration. For this study, we developed our own Monte Carlo simulation code based on ANSI C (see also Section 2.6).

2.2. Maximum-likelihood expectation–maximization (MLEM) algorithm

The counts registered by the detector pairs in coincidence are represented by the vector $y(j) = [y(1), y(2), y(3), ..., y(J)]$, where J is the total number of detector pairs allowed to detect coincidences defining a line of response (LOR). If K is the number of detector crystals on the ring, then $J = K(K − 1)/2$ is the total number of detector pairs in coincidence. If I is the number of pixels in the image vector **x**, the probability $P(\mathbf{y}|\mathbf{x})$ of observing $y(j)$ is a likelihood function $L(\mathbf{x})$ of the unknown emissions $x(i)$. The variables $y(j)$ are independent and Poisson distributed, with expectation $\tilde{y}(j)$, where:

$$\tilde{y}(j) = E[y(j)] = \sum_{i=1}^{I} x(i)\alpha(i,j) \tag{1}$$

The transition matrix $a(i,j)$ represents the probability for an event generated in the area of the source covered by pixel i to be detected by LOR j. Since $x(i)$ are independent Poisson variables, a linear combination of these variables as the one in the above equation is also Poisson distributed. Considering the above, the likelihood of the observed data is:

$$L(x) = P(y|x) = \prod_{j=1}^{J} e^{-\tilde{y}(j)} \frac{\tilde{y}(j)^{y(j)}}{y(j)!} \tag{2}$$

The likelihood function $L(\mathbf{x})$ expresses the Poisson probability to observe the given counts in detector pairs in coincidence if the true density is $x(i)$. Combining the Eqs. (1) and (2) the log-likelihood function is produced [6]:

$$l(\mathbf{x}) = \log(L(\mathbf{x})) = -\sum_{j=1}^{J}\sum_{I=1}^{I} x(i)a(i,j) + \sum_{j=1}^{J} y(j)\log\left(\sum_{i=1}^{I} x(i)a(i,j)\right)$$
$$- \left(\sum_{i=1}^{I} \log(y(j)!)\right) \tag{3}$$

In the MLEM algorithm the estimate of the image vector that maximizes $L(\mathbf{x})$ is the maximum-likelihood estimate of **x** given **y**. In other words, the problem of image reconstruction in PET is to estimate or guess the true unobserved counts x in each pixel taking into account the observed counts y in all detector pairs in coincidence. The application of maximum-likelihood estimation techniques in (3) leads to an expression for the update of the ith pixel at iteration $(k + 1)$ as follows:

$$x^{(k+1)}(i) = x^{(k)}(i)C^{(k)}(i) \tag{4}$$

where $C^{(k)}(i)$ is the updating coefficient and depends on the data of measured counts **y** and the forward projection of the estimated image vector **x** at iteration k, as well as on the transition matrix $a(i,j)$:

$$C^{(k)}(i) = \frac{1}{\sum_{j=1}^{J} \alpha(i,j)} \sum_{j=1}^{J} \frac{y(j)}{\sum_{i=1}^{I} \alpha(i,j)x^{(k)}(i)} \alpha(i,j) \qquad (5)$$

Solving the Eqs. (4) and (5), the EM algorithm can be expressed as:

$$x^{(k+1)}(i) = \frac{1}{\sum_{j=1}^{J} \alpha(i,j)} x^{(k)}(i) \sum_{j=1}^{J} \frac{y(j)\alpha(i,j)}{\sum_{i=1}^{I} x^{(k)}\alpha(i,j)}, \, i = 1, 2, ..., I \qquad (6)$$

Analyzing Eq. (6), the MLEM algorithm can be described in three steps:

(a) Start with an initial estimate $x^{(0)}$, where $x^{(0)}(i) > 0$ for $i = 1, 2, 3, ..., I$.
(b) If $x^{(k)}$ denotes the estimate of x at the kth iteration, calculate a new $x^{(k+1)}$ by Eq. (6).
(c) If the resulting image quality offers an acceptable result then stop, else return to (b).

For the above iterative scheme a robust stopping criterion is necessary, which would allow the selection of the reconstructed image with a good signal-to-noise quality among the set of the images produced by the iterative procedure. This iteration algorithm must be stopped after some iterations because if more likelihood is desired, after a certain optimum point the resulting images become noisier [11]. For this study, the MLEM algorithm was developed by our group employing ANSI C.

2.3. The transition matrix

The calculation of the transition matrix was done by employing Monte Carlo (MC) simulation techniques. MC technique was preferred because it is not so complicated such as analytical methods which are also used in the calculation of transition matrix [18]. Each matrix element $a(i,j)$ represents the transition law from the image activity distribution $x(i)$ to the measured data (detected counts) $y(j)$. It therefore represents the geometrical acceptance of annihilation events generated in pixel i, as they are detected in the detector pair j. Clearly, then, the transition matrix depends on the geometry of a PET scanner, namely, on the image grid and the scanner layout.

For the calculation of the transition matrix elements annihilation ($e^+ + e^- = \gamma + \gamma$) events are generated uniformly inside the area of the source covered by pixel i, producing gamma ray pairs distributed isotropically in space. These gamma rays are propagated to the scintillation detectors on the PET camera ring. The gamma rays are produced back-to-back forming a straight line. The intersection of this line with the scanner detectors defines which two detectors will be set in time coincidence. A success is characterized by a coincidence detection of the two gammas by the gamma ray detectors forming the detector pair j. The transition matrix element, $a(i,j)$ is computed by the following expression:

$$\alpha(i,j) = \frac{N_{ij}}{N_{tot}} \qquad (7)$$

where N_{ij} is the number of gamma rays emitted from a specific pixel i and detected by the detectors in pair j, and N_{tot} is the total number of gamma ray pairs emitted from this pixel i. In other words the matrix element $\alpha(i,j)$ characterizes the geometrical acceptance of a given detector pair j with respect to the source of annihilation at image pixel i. A different matrix has been calculated for all image grids employed in this work. In each case 10^7 gamma rays per pixel have been simulated, resulting in a minimum relative error (worst case) less than 1%.

2.4. PET image generation

For the study of the behavior of the update coefficients **C** in the MLEM algorithm, two sets of digital phantoms were used. The first is the MOBY phantom (129 2D slices) [19] and the second consists of 18 2D slices from the digital Hoffman brain phantom [20]. One characteristic slice from each phantom is shown in Fig. 1. For each one of the phantoms employed, simulated data sets at different activity distribution levels have been generated using Monte Carlo methods. The Digimouse phantom [21] was used for the validation of the method.

A dedicated algorithm was developed for the generation of annihilation events of the phantom active areas, in accordance with the physics of positron emission. The number of the generated events in each pixel was proportional to the pixel values of each phantom slice. Each annihilation event leads to the production of a pair of gamma rays, emitted isotropically in space in opposite directions. Once a gamma-pair is produced, it is allowed to propagate to the scanner detecting elements. The detection efficiency of each coincidence detector pair is assumed to be 100%. Monte Carlo generated lines of response form therefore the simulated "measurements" of the scanner. The MLEM algorithm has been used to reconstruct the corresponding image and this reconstructed image has been compared with the source phantom.
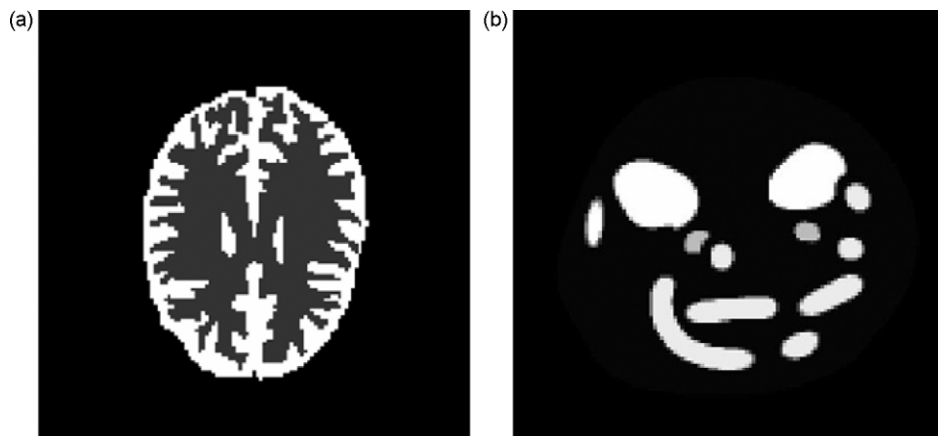

Fig. 1. (a) Slice No. 9 of Hoffman Brain phantom and (b) slice No. 65 of MOBY phantom.

2.5. Image quality figure of merit (FOM)

For the comparison of **x** and $\hat{\mathbf{x}}$ (the reconstructed and true image (phantom), respectively) the difference image $\mathbf{x} - \hat{\mathbf{x}}$ is studied. This could be done by examining the difference pixel by pixel, or by comparing corresponding groups of pixels in a selected region of interest (ROI) or by forming global quantities involving all the pixels. Such global quantities may be constructed from the sum of squares of the differences of the values (deviations) of each pixel, namely

$$\sum_{i=1}^{I} (x(i) - \hat{x}(i))^2.$$

Two such quantities have been employed in this work:

2.5.1. The normalized root mean square deviation (NRMSD)

From the definition of the root mean square deviation (RMSD):

$$\text{RMSD} = \sqrt{\frac{\sum_{i=1}^{I}(x(i) - \hat{x}(i))^2}{I}} \tag{8}$$

where I is the total number of pixels, and dividing by the RMS of $\hat{\mathbf{x}}$, namely by:

$$\text{RMS} = \sqrt{\frac{\sum_{i=1}^{I}\hat{x}(i)^2}{I}}$$

a new quantity can be defined that is called here normalized root mean square deviation (NRMSD) and is expressed as:

$$\text{NRMSD} = \sqrt{\frac{\sum_{i=1}^{I}(x(i) - \hat{x}(i))^2}{\sum_{i=1}^{I}\hat{x}(i)^2}} \tag{9}$$

The denominator in this expression is a fixed quantity (the total number of counts in the true image) that normalizes NRMSD to values between 0 and 1.

2.5.2. The chi-square χ^2

We define the quantity χ^2 as follows:

$$\chi^2 = \frac{2}{I}\sum_{i=1}^{I}\frac{(x(i) - \hat{x}(i))^2}{x(i) + \hat{x}(i)} \tag{10}$$

This provides a more accurate comparison that can be achieved by weighting the difference $(x(i) - \hat{x}(i))^2$ by the inverse of the variance of the difference, which in the case of Poisson statistics is just $x(i) + \hat{x}(i)$. In this case, differences with large statistical errors would contribute less to the summation in (10) and differences with small statistical errors should contribute more. In the present study both indicators have been used, namely the NRMDS and the χ^2.

It should be stressed at this point that these image comparisons are not unique and the choice of the method has to do with the objectives of the image analysis at hand. In the case of image reconstruction from measured projection data it is obvious that the activity distribution in the true image is not available. Therefore for real data a figure of merit based on image differences cannot be used. In contrast, in the special case of Monte Carlo simulation when one starts with a phantom and simulates the image acquisition process, followed by image reconstruction, one ends up with both quantities x and $\hat{\mathbf{x}}$. In this case, a single index of quality (a single FOM) can be used to characterize the image quality at a given iteration.

2.6. Software and hardware requirements

The Monte Carlo simulation as well as the reconstruction algorithm was coded in ANSI C. We used the free software ROOT v4.0/08 [22] for the image analysis. The computer program run in a Pentium 4, with 3.0 GHz CPU and 1.5 GB RAM which used the Microsoft Windows XP, Version 2002. For image size of 128×128 the calculation of the transition matrix required memory equal to 532 MB. The size of the produced transition matrix was 1.11 GB. Due to its large size, the stored transition matrix was coded in three different matrices. One was about the pixel i, one about the line of response j – where the emitted gamma rays from pixel i were detected – and one matrix in which the value for a specific pair i,j was stored. The total size of the three new matrices was 56.5 MB (16.1 + 14.9 + 25.5 MB). The total time which was needed for the calculation of transition matrix and its re-storing in three different matrices is almost 105 h.

3. Results and discussion

3.1. Quality of the reconstructed image versus number of iterations

Fig. 2 shows the log-likelihood, the NRMSD, and χ^2 as a function of the number of iterations for slice 14 of the Hoffman phantom. The log-likelihood increases slowly, after a rapid phase during the initial iterations, towards its maximum. Both image quality FOMs initially decrease up to some iteration, implying an improvement in image at each step during this early phase, and then they show an increase indicating the onset of image deterioration. We have studied the relationship among these two FOMs. In Fig. 3 the NRMSD versus the corresponding χ^2 is plotted for various slices of the Hoffman phantom and for various activity levels. It is clear that there is a one-
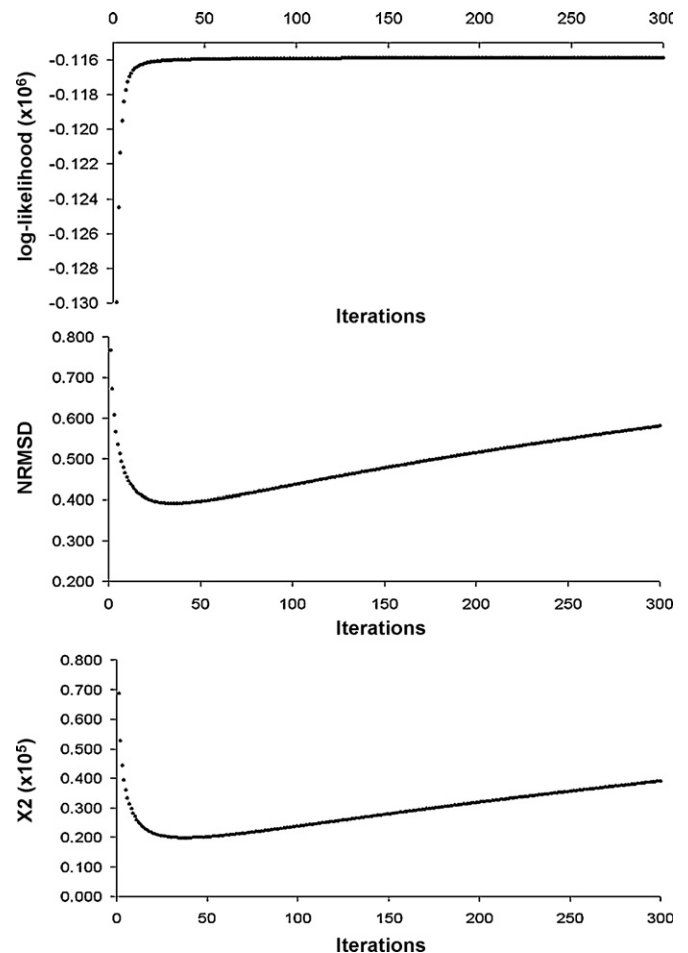

Fig. 2. Reconstruction of the Hoffman phantom slice #14 with 2.1 M counts activity: plots of the log-likelihood function, normalized RMS distance (NRMSD) and χ^2, versus iteration number.
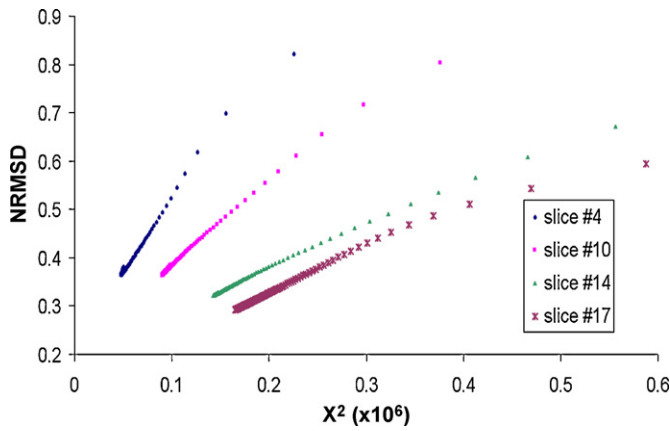
Fig. 3. NRMSD versus χ^2 for Hoffman slices #4, #10, #14 and #17 with activity 500k, 1 M, 2.1 M and 3.2 M counts respectively.

Fig. 4. NRMSD versus number of iterations for Hoffman slice #14 with activities of 200k, 1 M, and 4 M counts.

to-one correspondence between NRMSD and the corresponding χ^2. We can draw the conclusion that the use of only one of the three quantities is enough for the characterization of the image quality. The log-likelihood cannot be used at it monotonically increases. On the other hand NRMSD and χ^2 are better indicators having linear relationship between them. We select to use the NRMSD, since similar quantities (MSE, RMS) have been used by many authors to characterize image quality in image reconstruction algorithms [10,23–26].

We should stress the differences of the use of NRMSD in image reconstruction as compared to the use of MSE and RMS and image analysis. RMS may not be the best FOM of image quality when the objective is to study and compare features of an image related to a specific diagnostic task or other properties of the underlying methods employed. In such cases researchers may use other FOMs, for example detectability, contrast, spatial resolution [27]. In image reconstruction, however, where the image starts deteriorating due to added noise after a number of iterations, NRMSD or χ^2 can be an indicator of the iteration at which the iterative process must be halted in order to have the best signal-to-noise characteristics possible in the result obtained.

For studies based on Monte Carlo simulations the activity density vector x is known for both the true (phantom) and the reconstructed images and hence it is possible to compute image differences. In the case of image reconstruction with real (measured) projection data the NRMSD or χ^2 are not possible to be computed. In this case it is necessary to find and develop an image quality index based only on the inherent properties of the collected data. Such an index should accurately reflect the properties of the (unobservable) NRMSD. In this work Monte Carlo generated 2D datasets are employed and iteratively reconstructed using the MLEM algorithm, as discussed in the previous sections. The iteration where the optimum NRMSD occurs is recorded, along with the corresponding minimum value of the updating coefficients **C** for this iteration. The NRMSD is plotted in Fig. 4 as a function of the number of iterations for various activity distribution levels. The plot shows that the image quality, as expressed by the NRMSD, improves quickly in the beginning, followed by a wide minimum and subsequent deterioration. Fig. 4 shows that the NRMSD has its minimum value at iterations 35, 99, and 248 corresponds to 200k, 1.0 M and 4.0 M counts respectively. The variation of the NRMSD around the regions of the minima is less that 1% over a range of about 50 or so iterations, as image activity increases. In addition, this figure shows, based on the value of the NRMSD, that images with lower statistics $\bar{x}$ are of lower quality than the ones produced from data sets with a high total number of counts.
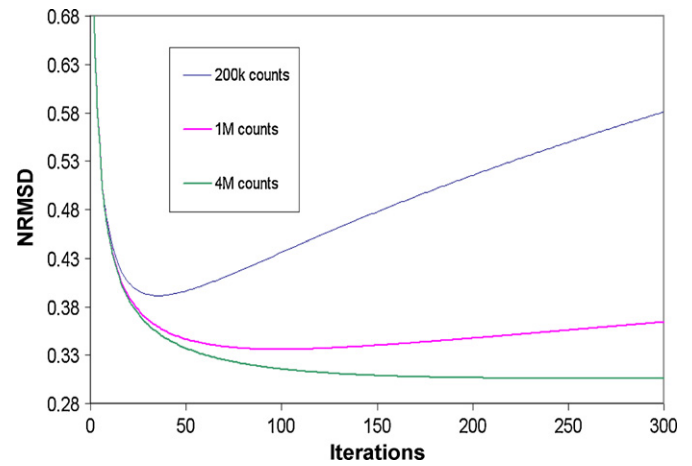
3.2. The variable C_{min} and its properties

From Eq. (4) it can be seen that the evolution of the coefficients **C** is responsible for the convergence rate as a function of the number of iterations. The behavior of the pixel updating coefficients **C** has been studied and analyzed in the present work. The updating coefficients for non-zero pixels in the true (phantom) image tend to reach a value around 1.0 after a large number of iterations. Therefore, it can be concluded that for pixel i the value of $C^{(k)}(i)$ will be tending to value 1.0, namely:

$$\lim_{k \to \infty} C^{(k)}(i) = 1.0 \tag{11}$$

On the other hand, the pixel updating coefficients **C** for the background (zero content) pixels do not converge to 1.0 but get values different than 1.0.

Motivated by the above observations we have studied further the evolution of the coefficients **C** for all non-zero pixels of the reconstructed image as the number of the iterations increases. Fig. 5 shows histograms, namely distributions of the values of the updating coefficients **C** for the Hoffman brain phantom slice 14 as a function of the MLEM iterations. These histograms correspond to the **C** values of the non-zero pixels in the phantom image. These histograms have two components:

1. one component around $C(i) = 1.0$ that corresponds to those pixels for which reconstruction is completed and
2. a tail, namely a region of $C(i) < 1.0$ that corresponds to pixels that need further iterations in order to reach their true value.

The tail distribution in the histograms shown in Fig. 5 with values lower than 1.0, corresponds to the part of the image that has not yet reached convergence. Such observation is also in line with the already proven fact that different regions in the reconstructed image have different convergence rates when algorithms such as the MLEM are employed. We show here that the minimum value of the tail is related to the noise characteristics of the reconstructed image. From these plots, it can be observed that as the iterative process progresses, two characteristics emerge:

1. the minimum of the tail distribution shifts to higher values close to 1.0, and
2. the Gaussian-like peak distribution around 1.0 becomes narrower and narrower.
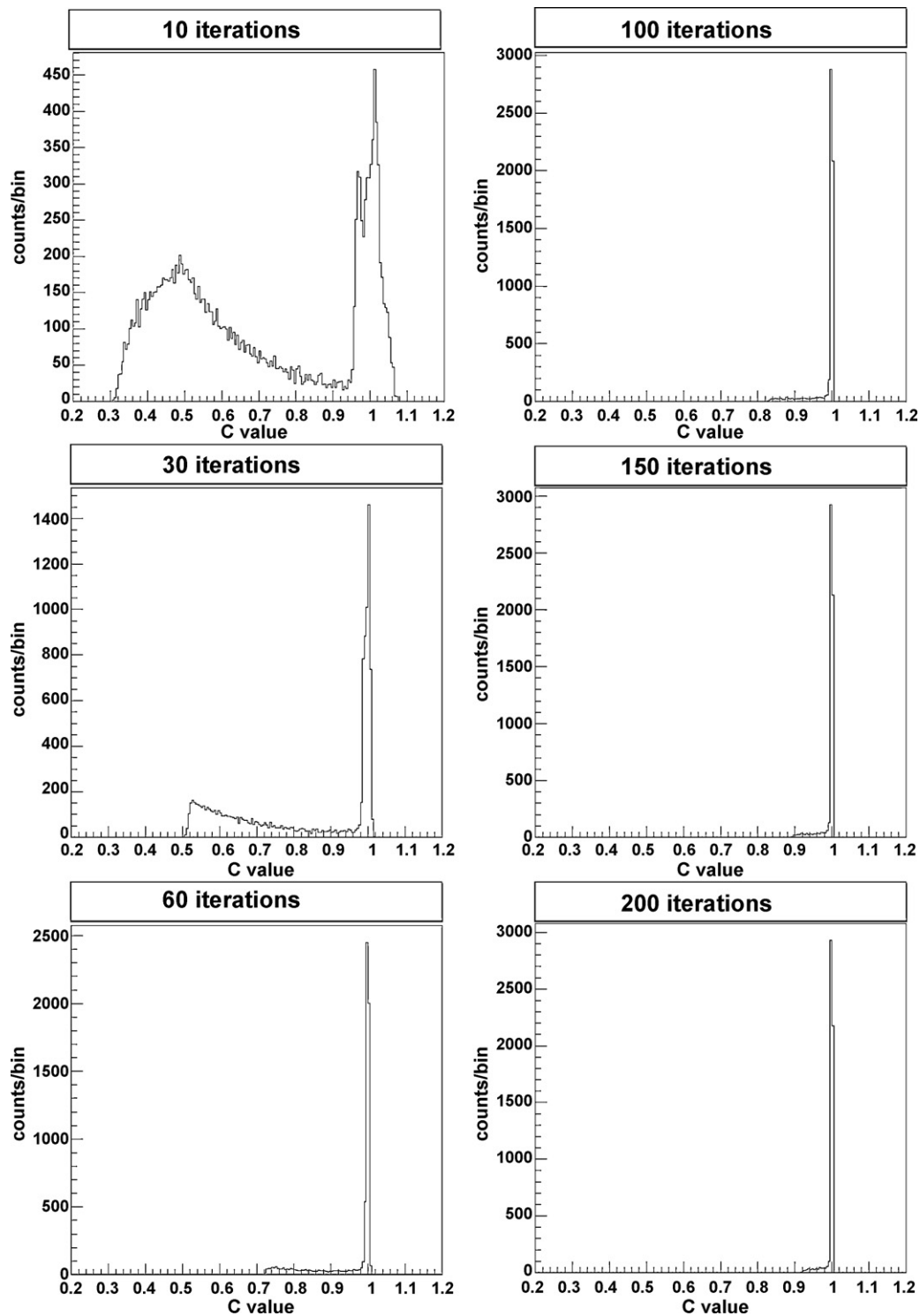
Fig. 5. Histograms of the updating coefficients C, at different iteration number of the reconstructed image for Hoffman slice No. 14. The leftmost value of C in each histogram is defined as C_{min}.

We define a vector variable: $C_{min}^{(k)} = \min\{C^{(k)}(i), \quad i = 1, \dots, I\}$, where I is the total number of pixels in the image and k is the iteration number. $C_{min}^{(k)}$ is the minimum value of the vector of the pixel updating coefficients $C^{(k)}(i)$ among the non-zero pixels in the reconstructed image at the current iteration k; $C_{min}^{(k)}$ can be read out easily from the corresponding histogram.

In this work we have studied the dependence of this variable on the iteration number and its relationship to the minimum NRMSD value. Fig. 6 shows the dependence of $C_{min}^{(k)}$ for Hoffman slice 14

for 2.1 M counts. It demonstrates that $C_{min}^{(k)}$ *increases monotonically* with the iteration number, showing thus a one-to-one correspondence between iteration number and $C_{min}^{(k)}$. We have studied the law of the dependence of $C_{min}^{(k)}$ on iteration number by fitting the data to variety of functions. The most successful has the following form:

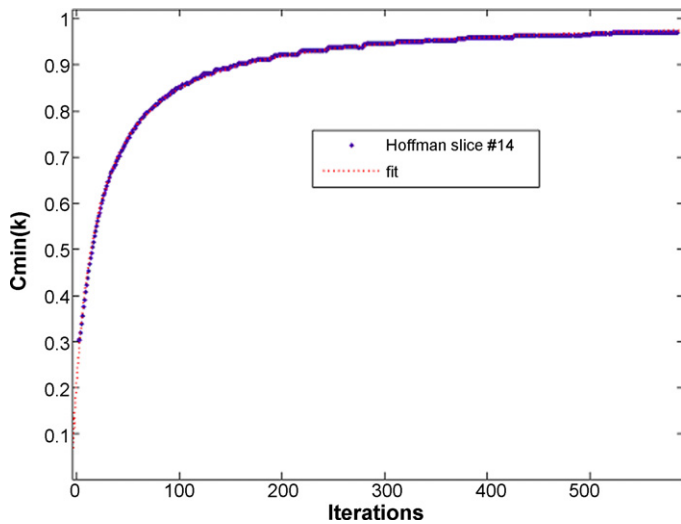$$C_{min}^{(k)} = A \frac{k + \alpha}{k + b} \tag{12}$$

Fig. 6. $C_{min}^{(k)}$ as a function of the number of iterations of Hoffman slice 14 for image of 2.1 M counts along with the fit by Eq. (12). The parameters of the fit are: $A = 1.01 \pm 0.002$, $\alpha = 4.22 \pm 0.326$, $b = 26.3 \pm 0.65$.

where k is the iteration number, and A, α, and b are constant parameters. The fitting curve is also shown in Fig. 6. The values of NRMSD and $C_{min}^{(k)}$ were recorded at every iteration and are plotted against each other in Fig. 7, for various image activities. This plot shows that, as $C_{min}^{(k)}$ increases, the NRMSD is decreasing up to the point when it reaches its minimum value, $NRMSD_{min}$, which corresponding to the image closest to the true one according to this FOM. For a given activity, there is a unique value of $C_{min}^{(k)}$ that signals the occurrence of the best achievable image in terms of NRMSD. Therefore following the evolution of $C_{min}^{(k)}$ we can specify the end of the iterative process. Fig. 7 shows that there is a weak dependence of the value of the minimum NRMSD as a function of $C_{min}^{(k)}$. This implies that $C_{min}^{(k)}$ at the best achievable image is not the same for all activity distribution levels. In images of low activity distribution levels higher values of minimum NRMSD are reached and lower $C_{min}^{(k)}$ values, while for images from high counts data the opposite is true.

The properties of the pixel updating coefficients described above allow tracking the image quality by following the value $C_{min}^{(k)}$ which can be calculated from the measured projections at each iteration.

3.3. Dependence of C_{min} on the image characteristics

In this section we examine the dependence of $C_{min}^{(k)}$ on several characteristics of the image: the image topology, the pixel size, and the image activity. In order to examine the dependence of image
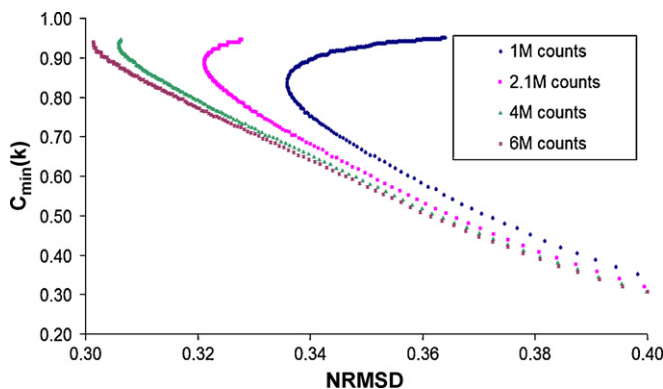

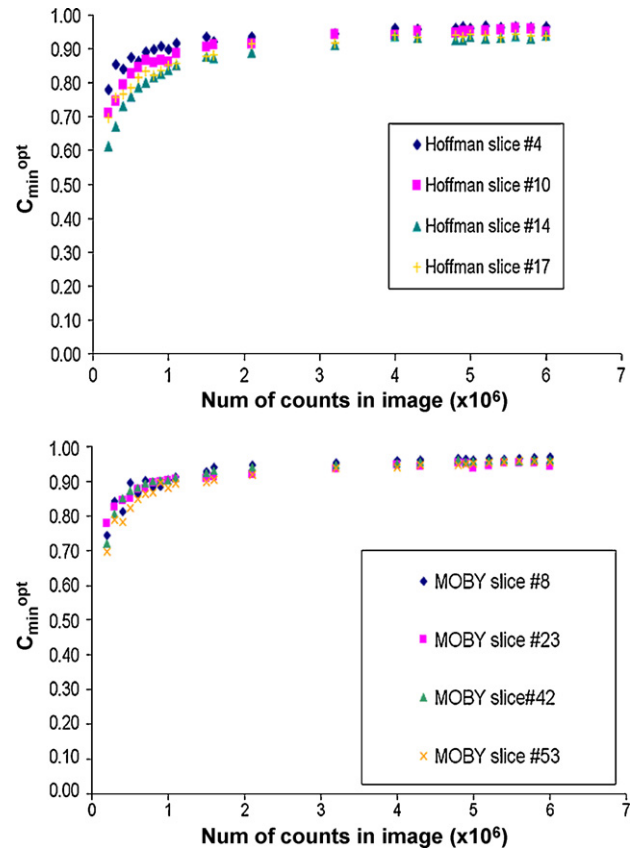**Fig. 7.** $C_{min}^{(k)}$ versus NRMSD for Hoffman slice 14 and for different image activities.

Fig. 8. C_{min}^{opt} as a function of image activity using the minimum NRMSD criterion for an image grid of 128×128. The slices were chosen as to provide maximum coverage of the image topology. (a) Slices #4, #10, #14 and #17 of the Hoffman phantom and (b) slices #8, #23, #42 and #53 of the MOBY phantom.

topology we generated and reconstructed images of various slices from the MOBY phantom and the Hoffman brain phantom. These slices allow a variety of topologies to be studied. The dependence on the activity level was studied with the above phantoms by generating and reconstructing images with a wide range of counts. In addition, a number of different pixel configurations were studied, in order to find out how the image grid might influence the results.

3.3.1. Dependence of $C_{min}^{(k)}$ on the image topology and activity level

We simulated the Hoffman and MOBY phantoms with a wide range from 0.2 to 6.0 M counts. Each image is reconstructed on an image grid of 128×128 pixels. For each activity we plotted the distribution of the values of the coefficients **C** and recorded the value of a new quantity C_{min}^{opt} namely the value of C_{min} at optimum image defined as follows:

$$C_{min}^{opt} \equiv \{C_{min}^{(k)}, \ k = \text{iteration at minimum NRMSD}\}$$

Fig. 8a shows the dependence of C_{min}^{opt} on the number of counts for the four slices 4, 10, 14 and 17 of the Hoffman phantom; whereas Fig. 8b shows the same dependence for the four slices 8, 23, 42 and 53 of the MOBY phantom. The plots in Fig. 8 show that:

(a) the value of C_{min}^{opt} (C_{min} at the best achievable image according to NRMSD) increases monotonically as a function of the number of counts,
(b) the dependence curves have similar shapes and
(c) there is a characteristic clustering of the values of C_{min}^{opt} for a given number of counts implying a very small dependence on the details of the images.
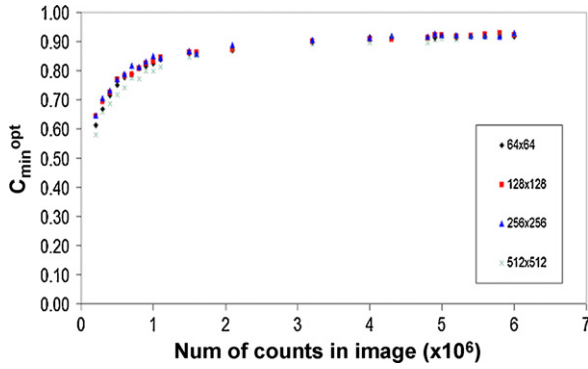
Fig. 9. $C_{\min}^{\text{opt}}$ versus the number of counts in the Hoffman slice No. 14 (for image sizes 64×64, 128×128, 256×256 and 512×512) using as image quality criterion the minimum NRMSD.

Therefore for an image with a given number of counts one can estimate from these plots the value of $C_{\min}^{\text{opt}}$. As previously discussed, for the reconstruction of images from real acquisitions, one can track the image quality by following the evolution of $C_{\min}^{(k)}$ as the reconstruction iterations proceed, until it reaches the value that corresponds to $C_{\min}^{\text{opt}}$ for the given number of counts. One can therefore stop the algorithm at that iteration.

3.3.2. Dependence of $C_{\min}^{opt}$ on the image grid

We have studied $C_{\min}^{\text{opt}}$ as a function of the number of counts for the same image and various image sizes from 64×64 to 512×512. The results of this study are shown in Fig. 9 for slice 14 of the Hoffman phantom. These plots show that the value of $C_{\min}^{\text{opt}}$ does not vary with the image grid size.

3.3.3. Parameterization of $C_{\min}^{opt}$ dependencies

In order to parameterize quantitatively the dependence of $C_{\min}^{\text{opt}}$ on the number of counts, we have fit the data of Fig. 8 (for all slices of each phantom) using several functional alternatives. The most successful parameterization has the form:

$$G = D\frac{N_c + \alpha}{N_c + \beta} \tag{13}$$

where N_c is the number of counts in millions. It should be noted that the data in Fig. 8 show a finite spread for a given number of counts. This spread is associated with the different topology of the images, which, as we have pointed out, has a rather weak effect. Therefore, to give a quantitative description of the dependence of $C_{\min}^{\text{opt}}$ on the number of counts, N_c, taking into account the uncertainty introduced by the image topology, we introduce a spread, or an uncertainty of the value of $C_{\min}^{\text{opt}}$. In other words we will talk about the mean behavior of $C_{\min}^{\text{opt}}$ as a function of the number of counts, N_c. For the estimation of the parameters D, α, and β, we perform the fitting using the weighted average and associated error of $C_{\min}^{\text{opt}}$ (Fig. 10).

The values of the fitted parameters D, α, and β are listed in Table 1 separately for the Hoffman and MOBY phantoms, along with the limits of $C_{\min}^{\text{opt}}$ for $N_c \to 0$ and for $N_c \to \infty$. The difference of the two limits at large N_c values is very small, about 0.01. Clearly both phantoms follow the same law. For this reason we have combined the
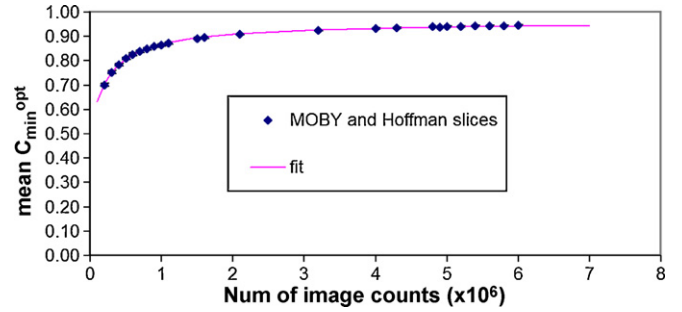

Fig. 10. The average values of $C_{\min}^{\text{opt}}$, over all slices of the Hoffman and MOBY phantoms, plotted versus image activity.
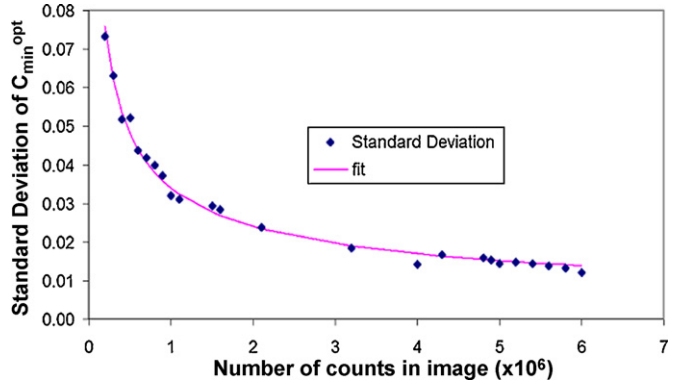

Fig. 11. The spread of the quantity $C_{\min}^{\text{opt}}$ (standard deviation) as a function of the image activity. The fitting equation has the form $A/\sqrt{N_c}$ where $A = 0.034 \pm 0.008$ and N_c is the number of counts in millions.

results obtained from both phantoms given in Fig. 8a and b. We have estimated the average values of $C_{\min}^{\text{opt}}$ at each activity and fit the result with Eq. (13). The resulting fit parameters are given in Table 1. As we noted before we have attempted several other functional parameterizations (e.g. polynomial, exponential, etc.) of the data. These fits were much less successful in comparison with that of Eq. (13). The spread of the values of $C_{\min}^{\text{opt}}$, around G, can be represented by the standard deviation σ, which has been estimated as a function of the image activity and plotted in Fig. 11. This spread was found to follow a functional dependence of the form:

$$\sigma = \frac{A}{\sqrt{N_c}} \tag{14}$$

showing clearly that the spread is of statistical nature and becomes smaller and smaller as the image activity increases, and represents the spread of the values of $C_{\min}^{\text{opt}}$ as seen in Fig. 8.

3.4. A stopping rule for the MLEM algorithm

Based on the previous analysis a stopping rule for the MLEM algorithm can be formulated, based on the variable $C_{\min}^{(k)}$ and the prediction of Eq. (13). From the measured projection data we can calculate $C_{\min}^{(k)}$ at every iteration and compare with the prediction G, of Eq. (13) for a given number of counts. The condition to stop

Table 1
Parameters of the of $C_{\min}$ fit for the Hoffman and MOBY phantoms.

Phantom	D	α	β	$C_{\min}$ ($N_c \to 0$)	$C_{\min}$ ($N_c \to \infty$)
MOBY	0.960 ± 0.003	0.130 ± 0.016	0.250 ± 0.022	0.50	0.96
Hoffman	0.970 ± 0.003	0.130 ± 0.020	0.250 ± 0.027	0.50	0.97
Both	0.960 ± 0.003	0.130 ± 0.016	0.250 ± 0.022	0.50	0.96

Table 2
The results of the reconstruction process of four Digimouse phantom slices.

Digimouse slice	Total counts	G	3σ	5σ	Stopping iteration $\lvert C_{min} - G\rvert \leq 3\sigma$	Stopping iteration $\lvert C_{min} - G\rvert \leq 5\sigma$	Iteration at minimum NRMSD
No. 27	1.349 M	0.8972	0.08790	0.14650	75	55	57
No. 59	2.180 M	0.9221	0.06921	0.11535	105	79	63
No. 97	1.686 M	0.9099	0.07866	0.13110	88	66	51
No. 127	2.570 M	0.9287	0.06376	0.10627	120	91	98

the MLEM algorithm would be therefore for $C_{min}^{(k)}$ to reach or exceed the value G, as predicted by Eq. (13). The scheme of the proposed stopping rule would be:

1. Knowing the total number of counts, predict the value of G using Eq. (13).
2. Compute the value of the pixel updating coefficients, $C^{(k)}(i)$ for all pixels $i = 1, \ldots I$, at iteration k.
3. Calculate the image vector $x^{(k+1)}(i) = x^{(k)}(i)C^{(k)}(i)$.
4. Compute $C_{min}^{(k)} = \min\{C^{(k)}(i)\}$.
5. Stop at iteration k for which the condition.

$$C_{min}^{(k)} \geq G \tag{15}$$

is met.

At this point we should deal with the small but finite spread of the values of $C_{min}^{(k)}$ shown in Fig. 8 and parameterized by Eq. (14). If the algorithm is stopped at the value of G then the various slices would be reconstructed at iterations around the minimum NRMSD. A more careful inspection of the plots of NRMSD versus iteration (Fig. 4), reveals that the NRMSD varies very slowly for iterations beyond the one at minimum NRMSD, and much faster before that iteration. Therefore, stopping the algorithm a little later after the minimum does not change appreciably the image quality. However care should be taken to prevent premature stopping before reaching minimum NRMSD due to the abrupt fall of the curve before this point. Having that in mind, the criterion in Eq. (14) can be relaxed as follows:

$$\lvert C_{min}^{(k)} - G\rvert \leq \delta \tag{16}$$
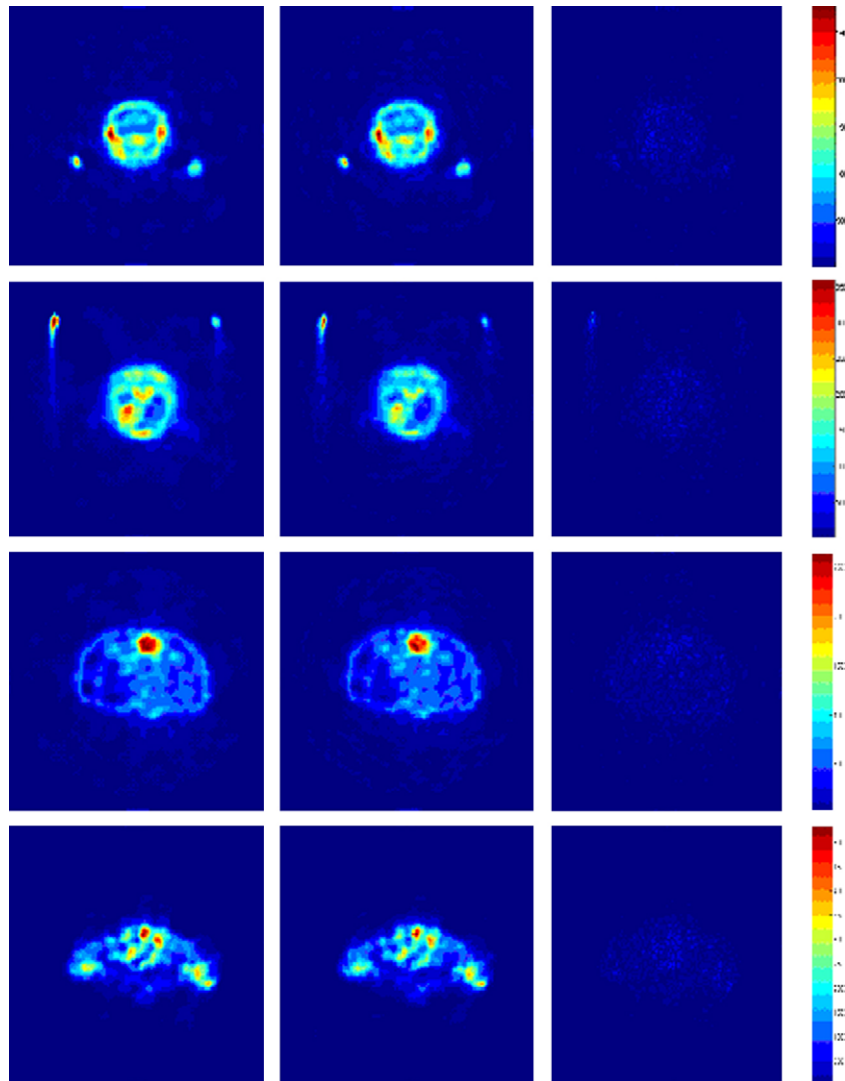

Fig. 12. Comparison of the source and reconstructed image using the stopping criterion of expressions 15 (see text). Left: source image, middle: reconstructed image, right: difference image for Digimouse phantom slices #27, #59, #97 and #127 respectively. The color scale is common to all three images for each slice.

where the limit δ can be expressed in terms of the standard deviation, σ. One choice can be $\delta = 3\sigma$, related to the fact that for a Gaussian distribution the distance of $\delta = 3\sigma$ from the mean G represents the 99.7% confidence level limit.

3.5. Validation of the stopping rule

The stopping criterion has been validated using a set of real (scanned) images from the Digimouse phantom [21]. Using these 2D images as inputs, we have generated projections using the Monte Carlo techniques applied in the previous cases and then used the MLEM algorithm for the reconstruction of these datasets, applying the stopping criterion given by inequality (16) to reconstruct all 2D slices. We present here the results from representative slices Nos. 27, 59, 97, and 127. Table 2 shows the number of counts for each slice, the critical value G, the iteration at minimum NRMSD along with the iterations at which the algorithm stops, and for which in inequality (16) holds for $\delta = 3\sigma$, and $\delta = 5\sigma$. Fig. 12 shows a comparison between the phantoms and the reconstructed images for $\delta = 3\sigma$. Plotted are the phantom image, the reconstructed image using the stopping rule and their difference in the same color code. As shown, the difference image (right column) in each slice is quite low in comparison to the maximum pixel value in each image. From this comparison, it can be observed that images produced by the proposed stopping criterion are close to the optimum images that the MLEM algorithm may produce.

4. Conclusions

The present paper is reporting the discovery of some interesting properties of the updating coefficients and their exploitation in forming an empirical and practical rule for stopping the MLEM algorithm. For this purpose, the behavior of the pixel updating coefficients, $\mathbf{C}$, was analyzed extensively. The values of $\mathbf{C}$ for non-zero pixels follow a distribution with a tail that moves towards the value of 1.0 as the iteration proceeds. Using Monte Carlo generated source images, a direct correlation of the minimum value, C_{min}, with the figure of merit, NRMSD, was observed. In other words C_{min}, estimated exclusively from the scanner data was found to be in a one-to-one correspondence with NRMSD. The value of C_{min} at minimum NRMSD is a function of the number of counts in the image and can be predicted by using Eq. (13). For acquired images, where NRMSD is not available, the estimated C_{min} is to be compared with the value G, given by Eq. (13). The decision to stop iterating is given by the inequality (16). This study was performed for different kinds of images and the behavior of $\mathbf{C}$ values was found to be the same. The minimum values of $\mathbf{C}$ are shown to be independent of the image size and nearly the same for different kind of images. The only parameter that seems to play a role in the behavior of $\mathbf{C}$ is the number of counts (activity) in each image. This study has been used to underline the principle and relies on Monte Carlo generated images. There are features that are not covered and which are under study:

(i) The effect of noise coming from absorption and scattering. In real PET scanners these effects should be first corrected before the algorithm gets applied. Because of the statistical nature of the introduced noise one has to take the necessary steps. This may involve applying a threshold to the values of the system matrix as well as to the scanner data.
(ii) The different geometry of PET scanners has an effect on the transition (system) matrix and the question whether the equation that predicts the critical value of K has the same parameters. This question can be resolved for a given scanner geometry by simulation studies, that need be performed only once during the commissioning period.

Work on the performance of the method in real data including all noise effects (attenuation, scatter, etc.) as well as for real clinical PET data is currently ongoing and will be the subject of a separate publication. This can be accomplished using a well-validated simulation code such as GATE [28]. Such software facilitates the simulation and measurement under realistic conditions the noise effects from physics and geometry. Subsequently the resulting sinogram will be corrected by subtracting the noise due to scattering, absorption and random effects. The resulting noise "free" projections will be used to reconstruct and study in the same way that we studied before. Alternatively, one can compute for each image pixel the Noise Equivalent Count Rate (NECR) and use it to study the properties of the image against activity. This will lead to a stopping rule which we shall compare with the noise-free case. The possibility of the optimization of Noise Equivalent Count Rate of the PET scanner due to stopping rule can be explored in the case of noisy data. The presented methodology can be extended to any imaging system using MLEM algorithm such as SPECT. Also, similar methodology can be implemented in the case of the OSEM algorithm.

References

[1] Juweid ME, Cheson BD. Positron-emission tomography and assessment of cancer therapy. Engl J Med 2006;354:496–507.
[2] Herholz K, Heiss WD. Positron emission tomography in clinical neurology. Mol Imag Biol 2004;6(4):239–69.
[3] Tarakji KT, Brunken R, McCathy PM, Al-Checakie O, Abdel-Latif A, Pothier CE, et al. Myocardial viability testing and the effect of early intervention in patients with advanced left ventricular systolic dysfunction. Circulation 2006;113:230–7.
[4] Frank R, Hargreaves R. Clinical biomarkers in drug discovery and development. Nat Rev Drug Discov 2003;2:566–80.
[5] Kontaxakis G. Positron emission tomography. Encyclopedia of medical devices and instrumentation, vol. 5, 2nd ed. Hoboken, New Jersey: John Wiley & Sons; 2006. p. 406–418.
[6] Shepp LA, Vardi Y. Maximul likelihood reconstruction for emission tomography. IEEE Trans Med Imag 1982;MI-1(2):113–21.
[7] Hudson M, Larkin RS. Accelerated image reconstruction using ordered subsets of projection data. IEEE Trans Med Imag 1994;13:601–9.
[8] Townsend DW. Physical principles and technology of clinical PET imaging. Ann Acad Med Singapore 2004;33(2):133–45.
[9] Hamill J, Bruckbauer T. Iterative reconstruction methods for high-throughput PET tomographs. Phys Med Biol 2002;47:2627–36.
[10] Chuang K-S, Jan M-L, Wu J, Lu JC, Chen S, Hsu CH, et al. A maximum-likelihood expectation maximization algorithm with thresholding. Comput Med Imag Graph 2005;29:571–8.
[11] Veklerov E, Llacer J. Stopping rule for the MLE algorithm based on statistical hypothesis testing. IEEE Trans Med Imag 1987;MI-6(4).
[12] Veklerov E, Llacer J, Hoffman EJ. MLE reconstruction of a brain Phantom using a Monte Carlo transition matrix and a statistical stopping rule. IEEE Trans Nucl Sci 1988;35(1).
[13] Holte S, Schmidlin P, Linden A, Rosenqvist G, Eriksson L. Iterative image reconstruction for positron emission tomography. IEEE Trans Nucl Sci 1990;37(2).
[14] Bissantz N, Mair BA, Munk A. A multi-scale stopping criterion for MLEM reconstruction in PET. In: IEEE medical imaging conference proceedings. 2006.
[15] Tzanakos G, Kontaxakis G. Statistical behaviour of the updating coefficient in the EM algorithm for PET. In: Conference record of the 1994 IEEE nuclear science symposium and medical imaging conference, vol. 3. 1994. p. 1310–4.
[16] Kontaxakis G, Tzanakos G. Stopping criterion for the iterative EM-MLE image reconstruction for PET. In: 1996 SPIE proceedings, vol. 2710. 1996. p. 133–44.
[17] Kontaxakis G, Straus LG, Tzanakos G. An efficient implementation of the iterative MLEM image reconstruction algorithm for PET on a Pentium PC platform. J Comput Inf Technol 1999;7(2):153–63.
[18] Loudos G. An efficient calculation of probability matrix in 2D SPECT. Comput Med Imag Graph 2008;(32):83–94.
[19] Segars WP, Tsui BMW, Frey EC, Johnson GA, Berr SS. Development of a 4D digital mouse phantom for molecular imaging research. Mol Imag Biol 2004;6(3):149–59.
[20] Hoffman EJ, Cutler PD, Digby WM, Mazziotta JC. 3D phantom to simulate cerebral blood flow and metabolic images for PET. IEEE Trans Nucl Sci 1990;NS-37(2):616–20.
[21] Dodgas B, Stout D, Chatziioannou AF, Leahy RM. Digimouse: a 3D whole body mouse atlas from CT and cryosection data. Phys Med Biol 2007;52:577–87.
[22] http://root.cern.ch/drupal/.
[23] Tsui BMW, Zhao X, Frey EC, Gullberg GT. Properties of iterative algorithms in SPECT image reconstruction. In: Conf. record, 1990 IEEE nuclear science symposium and medical imaging conference. 1990. p. 1467–74.
[24] Tanaka E. Intelligent iterative image reconstruction with automatic noise artifact suppression. In: Conf. record, 1990 IEEE nuclear science symposium and medical imaging conference. 1990. p. 1480–6.

[25] Stamos JA, Rogers WL, Clinthorne NH, Koral KF. Object-dependent performance comparison of two iterative reconstruction algorithms. IEEE Trans Nucl Sci 1988;35(1):611–4.
[26] Rehfeld N, Alber M. The influence of noise in full Monte-Carlo ML-EM and dual matrix reconstructions in positron emission tomography. Med Phys 2006;133(9):3498–507.
[27] Rafecas M, Mosler B, Dietz M, Pogl M, Stamatakis A, McElroy DP, et al. Use of a Monte Carlo-based probability matrix for 3-D iterative reconstruction of MADPET-II data. IEEE Trans Nucl Sci 2004;51(5):2597–605.
[28] Jan S, Santin G, et al. GATE: a simulation toolkit for PET and SPECT. Phys Med Biol 2004;49:4543–61.

Anastasios Gaitanis was born in Greece in 1976. In 2000, he obtained the BSc degree in Engineering of Medical Instruments Technology at the TEI of Athens in Greece. In 2001 he received the MSc degree in Medical Physics from the University of Surrey in UK. Since 2003 is at charge of Biomedical Technology Department of Biomedical Research Foundation of Academy of Athens (BRFAA). Since the middle of 2005 he is working on a PhD on PET image reconstruction under the supervision of the University of Patras and the collaboration of the University of Athens. His research interests are on biomedical image and signal processing, with more specific interests in image reconstruction based on PET and CT imaging systems.

George Kontaxakis is a tenured Contract Professor at the Department of Electronic Engineering of the Universidad Politécnica de Madrid, Spain. He holds a PhD degree in Biomedical Engineering joined from Rutgers, the State University of New Jersey and the University of Medicine and Dentistry of New Jersey, USA. He held various research positions in the German Cancer Research Centre in Heidelberg, the Fraunhofer Institute for Computer Graphics in Darmstadt, and the Macquarie University in Sydney. His main areas of interest are molecular image reconstruction, analysis and processing, medical informatics and eHealth applications. His research work has been published at more than 35 papers in peer-reviewed journals and book chapters, and over 100 scientific conference proceedings. George is a Senior Member of IEEE and Associate Editor of the IEEE Transactions on Information Technology in Biomedicine.

George Spyrou received his BSc on Physics from National and Kapodistrian University of Athens. He holds a Master of Sciences and a PhD on Medical Physics as well as a Master of Sciences on Bioinformatics. The main aim of Spyrou is the application of his knowledge and skills in Physics, Mathematics and Informatics to medically and biologically relevant issues, mainly on the 'mining' of the information either in direct medical data (e.g. medical images) or in genomes and proteomes relevant to medical problems.

George Panayiotakis was born in Chania, Greece, in 1956. He received his BSc in Physics (1979) and his PhD in Medical Physics (1986) from the University of Patras, Greece. He is a professor in the Department of Medical Physics, School of Medicine, University of Patras, Greece and head of the Medical Radiation Physics Unit at the University Hospital of Patras. He currently is the head of the Steering Committee of the Interdepartmental Program of Postgraduate Studies in Medical Physics and member of the Steering Committee of the Interdepartmental Program of Postgraduate Studies in Electronics and Information Processing, both offered by the University of Patras. He is a member of the Greek Federal Committee for Medical Physics licensing and consultant of the National Food and Drug Administration, Greece. He is a member of the overseas advisor committee of The British Journal of Radiology and reviewer in various international journals. He has published over 150 papers in international peer-reviewed journals and over 300 papers in international conferences. His research interests focus on medical imaging and include medical radiation physics, medical image detectors and simulation using Monte Carlo techniques, as well as medical image processing and analysis.

George Tzanakos is a Professor of Physics at the (National and Kapodistrian) University of Athens. He received his BSc (1964) in Physics from the University of Athens, Masters Degrees in Physics (1974) and in Computer and Information Science (1977), and a PhD in Physics (1976) all from Syracuse University, in Syracuse, New York, USA. He was a postdoctoral Research Associate and Research Assistant Professor at Syracuse University in the period 1976–1981, then faculty member in the Physics Department of Columbia University in the city of New York, in the period 1981–1990, and moved to the University of Athens in 1990. He has held, in parallel, various Visiting Professor/Scientist Appointments (BME department at Rutgers, the State University of New Jersey, USA, Fermilab in Batavia, Illinois, USA, Physics Department of the University of Cyprus, Nicosia, Cyprus). His interests include research in Medical Imaging, specifically in PET tomograph design and construction, Image Reconstruction, Mammography, Multimodality Imaging, and Monte Carlo Simulations. In parallel, he is pursuing research in elementary particle physics in National Laboratories (Brookhaven, Fermilab, SLAC, and CERN). He and his research group have contributed to research in fundamental problems in neutrino physics with particle accelerators, resulting in the discovery of the tau-neutrino and the observation of the phenomenon of neutrino oscillations. He has served as Director of Undergraduate Labs at Columbia and Athens Universities. He has published over 140 papers in professional journals and conference proceedings in Engineering and Physics. He is serving as a reviewer in several physics and engineering international journals, and also as an organizer in several International Conferences (IEEE EMBS, IEEE NSS @ MIC, WIN05, Neutrino-2010).